Journal of Applied Physics

RESEARCH ARTICLE | MARCH 26 2025

Thermal performance of materials for heat-assisted magnetic recording

Special Collection: Disordered Materials at the Atomic Scale

Xiaotian Xu ; Chi Zhang ; Silu Guo ; Nicholas C. A. Seaton ; K. Andre Mkhoyan ;
Joseph Roth ; Jie Gong ; Xuan Zheng; Neil Zuckerman ; Xiaojia Wang

J. Appl. Phys. 137, 125111 (2025)
https://doi.org/10.1063/5.0258288

Articles You May Be Interested In

A study of Ta_2O_5 photonic crystals waveguide for Heat-Assisted Magnetic Recording (HAMR)

AIP Conf. Proc. (August 2023)

A comparative analysis of Ag and Cu heat sink layers in L1-FePt films for heat-assisted magnetic recording

J. Appl. Phys. (April 2011)

SNR improvement by variation of recording and media parameters for a HAMR exchange coupled composite media

AIP Advances (January 2018)

AIP Publishing

Journal of
Applied Physics

ARTICLE

pubs.aip.org/aip/jap

Thermal performance of materials for heat-assisted magnetic recording

Cite as: J. Appl. Phys. **137**, 125111 (2025); doi: 10.1063/5.0258288
Submitted: 15 January 2025 · Accepted: 5 March 2025 ·
Published Online: 26 March 2025

Xiaotian Xu,[1] Chi Zhang,[1,a)] Silu Guo,[2] Nicholas C. A. Seaton,[3] K. Andre Mkhoyan,[2] Joseph Roth,[4] Jie Gong,[4] Xuan Zheng,[4] Neil Zuckerman,[4] and Xiaojia Wang[1,a)]

AFFILIATIONS

[1]Department of Mechanical Engineering, University of Minnesota, Minneapolis, Minnesota 55455, USA
[2]Department of Chemical Engineering and Materials Science, University of Minnesota, Minneapolis, Minnesota 55455, USA
[3]Characterization Facility, University of Minnesota, Twin Cities, Minneapolis, Minnesota 55455, USA
[4]Seagate Technology LLC, Bloomington 55435, USA

Note: This paper is part of the special topic on Disordered Materials at the Atomic Scale.
[a)]**Authors to whom correspondence should be addressed:** zhan6019@umn.edu and wang4940@umn.edu

ABSTRACT

To increase the storage capacity of hard disk drives, Heat-Assisted Magnetic Recording (HAMR) takes advantage of laser heating to temporarily reduce the coercivity of recording media, enabling the writing of very small data bits on materials with high thermal stability. One key challenge in implementing HAMR is effective thermal management, which requires reliable determination of the thermal properties of HAMR materials over their range of operating temperature. This work reports the thermal properties of dielectric (amorphous silica, amorphous alumina, and AlN), metallic (gold and copper), and magnetic alloy (NiFe and CoFe) thin films used in HAMR heads from room temperature to 500 K measured with time-domain thermoreflectance. Our results show that the thermal conductivities of amorphous silica and alumina films increase with temperature, following the typical trends for amorphous materials. The polycrystalline AlN film exhibits weak thermal anisotropy, and its in-plane and through-plane thermal conductivities decrease with temperature. The measured thermal conductivities of AlN are significantly lower than that which would be present in single-crystal bulk material, and this is attributed to enhanced phonon-boundary scattering and phonon-defect scattering. The gold, copper, NiFe, and CoFe films show little temperature dependence in their thermal conductivities over the same temperature range. The measured thermal conductivities of gold and copper films are explained by the diffuse electron-boundary scattering using an empirical model.

I. INTRODUCTION

Heat-Assisted Magnetic Recording (HAMR) is an advanced data-storage technology used in hard drives to significantly increase storage capacity by boosting the areal density of data. Widely studied in recent years, HAMR has recorded data at densities beyond the limits of conventional perpendicular magnetic recording (PMR).[1,2] A schematic of the HAMR writing process is shown in Fig. 1.[3] The recording medium consists of a granular magnetic material, and the grains' magnetization states will be periodically altered by the magnetic field from the writing pole. The magnetization directions (up and down) represent the binary data (0 or 1).[4] A key distinction between HAMR and the conventional PMR is the addition of a laser employed for local and temporal heating. The writing process in HAMR involves locally heating the magnetic medium close to or above the Curie temperature T_c, typically in the range of 400–500 °C, to reduce the material's coercivity. As the medium cools below the Curie temperature, the applied head field writes data. The subsequent cooling process further increases coercivity, ensuring the stability of the written data.[1] Specifically, a near-field transducer (NFT) is used to heat the medium, with the laser spot size confined to tens of nanometers, well below the diffraction limit. This heating, writing, and cooling operation proceeds bit-by-bit down a data track as the disk spins under the HAMR hard drive's recording head.

The signal-to-noise ratio (SNR) sensed during the readback of a magnetic data track depends on the number of grains per bit, and smaller data bits require smaller magnetic grains to maintain an

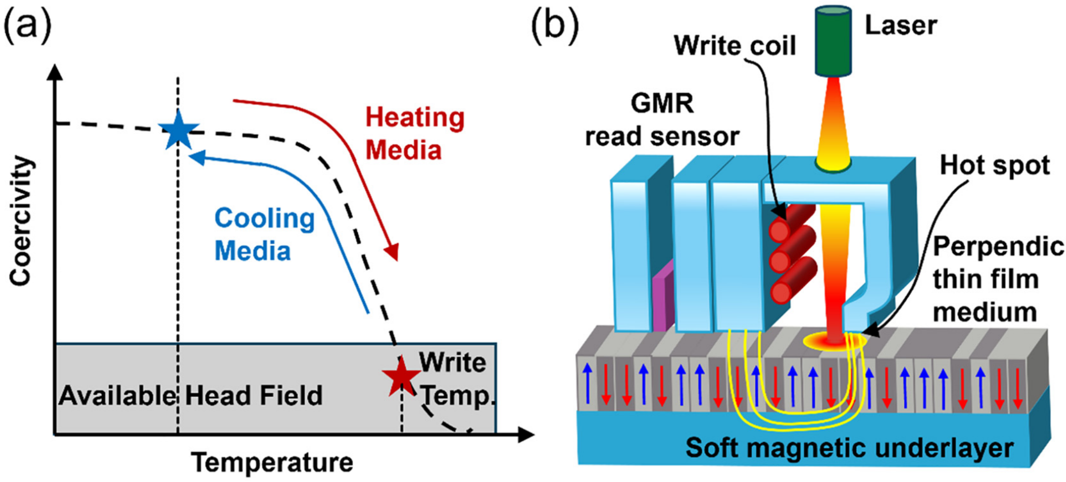

FIG. 1. (a) Working principles of heat-assisted magnetic recording. Adapted from Ref. 3 with permission of AIP Publishing LLC.[3] (b) HAMR schematic.

acceptable SNR. In addition, a smaller bit size is also favored to reach a competitive data-storage density. The size of each magnetic data bit is ultimately controlled by the size of the hot spot on the HAMR recording medium. Only the region heated by the NFT changes its direction of magnetization as the magnetic writer switches the external field. The temperature gradients present at this spot ultimately define the minimum size of the data bit.

This complex system introduces new thermal and magnetic challenges in hard-drive engineering. The laser irradiation of a plasmonic material (e.g., gold) will cause excessive heating, potentially leading to thermally driven deformation or failure. This results in an obvious need for thermal management in a recording head, where local heat fluxes are extremely high. The recording medium also needs to have a heat-sinking design that enables rapid heating and cooling within the nanosecond time scale. Thus, a comprehensive understanding of the thermal properties of HAMR materials over the operating temperature range is essential to guide the design and optimization of HAMR.

In this work, we perform a systematic study of the temperature-dependent (*T*-dependent) thermal properties of key HAMR materials produced by Seagate, including dielectric films of silica, alumina, and aluminum nitride, metallic films of gold and copper, and magnetic alloys of CoFe and NiFe thin films. Using time-domain thermoreflectance (TDTR) measurements, the *T*-dependent through-plane (Λ_z) and in-plane (Λ_r) thermal conductivities of the samples are measured from room temperature (RT) to 500 K. The extracted material properties will improve the understanding of thermal transport in these thin-film HAMR materials and provide valuable insights for further improving HAMR design and performance.

II. SAMPLE FABRICATION AND CHARACTERIZATION

The thin-film samples in this study were produced by Seagate, a manufacturer of HAMR recording heads, media, and drives. For instance, amorphous dielectric silica and alumina are commonly used as optical materials in HAMR. Amorphous alumina also serves as an electrically insulating encasing material due to its mechanical properties. Copper is a common choice for electromagnet coils in both HAMR and PMR heads, and it is also an excellent heat conductor. Gold is the most studied plasmonic material for HAMR, and similar to copper, it also can provide excellent heat dissipation. Aluminum nitride (AlN), known for its relatively high bulk thermal conductivity ($\sim$330 W m^{-1} K^{-1}),[5–10] is widely used for heat dissipation in locations where electrical isolation is required. Magnetic alloys CoFe and NiFe are commonly used as write-pole materials for HAMR heads. $Co_{0.35}Fe_{0.65}$ possesses a high saturation magnetization (reaching 2.45 T), making it favored for write-pole tips. $Ni_{80}Fe_{20}$, also known as Permalloy or "80–20," can serve as a material for return poles, shields, and other magnetic features in the head.

All samples were prepared by Seagate using microfabrication processes such as sputtering, reactive deposition, plasma-enhanced chemical vapor deposition (PECVD), and electroplating. $Co_{0.33}Fe_{0.67}$ films were produced by depositing a Cr adhesion layer and a Cu plating seed onto a thermally oxidized Si wafer, covering these films with a 30 nm $Co_{0.30}Fe_{0.70}$ seed layer, and then electroplating 300 nm of $Co_{0.33}Fe_{0.67}$ alloy onto the seed layer. Thin Cr films were used as adhesion layers for the sputtered Cu and Au films, produced on thermally oxidized Si wafers. All other films were produced on Si substrates using vacuum deposition techniques. Bare Si and thermally oxidized SiO_2/Si wafers were also provided by Seagate as reference samples, permitting isolation of the substrate effects on the measured sample properties. The composition of amorphous silica was close to that of SiO_2 but not exactly stoichiometric. Likewise, the composition of amorphous alumina was close to that of Al_2O_3. The thicknesses of all thin-film samples were characterized using scanning electron microscopy (SEM). High-angle annular dark-field scanning transmission electron microscopy (HAADF-STEM) and x-ray diffraction (XRD) were also used to understand the microstructures of polycrystalline

TABLE I. Sample stack structures and related HAMR applications.

Category	Sample stack information (thickness in nm)	Fabrication processes	Structural features	HAMR applications
Alumina	Alumina (1000)/Si	Sputtering	Amorphous	Cladding materials for plasmonics and optics; interlayers
Silica	Silica (192)/Si	PECVD	Amorphous	
Aluminum nitride (AlN)	AlN (364)/Si	Reactive deposition	Polycrystalline	Electrical isolation; heat sink
Gold (Au)	Au (46)/Cr (5)/SiO_2 (288)/Si	Sputtering	Polycrystalline	Plasmonic NFT; heat sink; head coils
Copper (Cu)	Cu (101)/Cr (5)/SiO_2 (192)/Si	Sputtering	Polycrystalline	
Nickel-iron (NiFe)	$Ni_{80}Fe_{20}$ (104)/SiO_2 (294)/Si	Sputtering	Polycrystalline	Write poles of heads; magnetic shields
Cobalt-iron (CoFe)	$Co_{0.33}Fe_{0.67}$ (300)/$Co_{0.30}Fe_{0.70}$ (30)/Cu (198)/Cr (29)/SiO_2 (313)/Si	Electroplating	Polycrystalline	

films. Table I summarizes the sample information, fabrication processes, structural features, and related HAMR applications.

III. THERMAL MEASUREMENTS AND DATA REDUCTION

Because the HAMR recording head must withstand and operate at elevated temperatures, it is essential to understand the thermal properties of these materials under such conditions. We used the state-of-the-art ultrafast pump-probe technique, TDTR, to measure the thermal conductivities (Λ) of thin-film samples from RT to 500 K. For samples exhibiting thermal anisotropy, both the through-plane Λ_z and in-plane Λ_r were examined. Before thermal measurements, a thin metallic layer (e.g., Al or Pt) was sputtered onto the sample (e.g., alumina, silica, AlN, or CoFe) as a transducer. This procedure was also performed with the 300 nm SiO_2/Si control samples. For the Au, Cu, and NiFe thin films, the material to be tested served as the transducer layer. In TDTR (Fig. 2), a pump laser beam heats the sample stack, causing a temperature rise at the transducer surface, followed by a cooling process. A probe beam illuminates the sample stack at a varying time delay. The reflectivity of the probe beam varies with the temperature of the transducer surface due to the thermoreflectance effect.[11,12] For a small temperature rise, the variation in the probe reflectivity is linearly proportional to the temperature excursion between pump heating and probe sensing and, thus, provides thermal information about the sample stack.[11,13,14] More details of the TDTR metrology can be found in other publications.[11,13–23] The experimental data were compared to a 3D heat transfer model to extract the thermal properties of interest.[24]

For through-plane thermal measurements, the thermal wave propagation in the sample stack due to the modulated pump

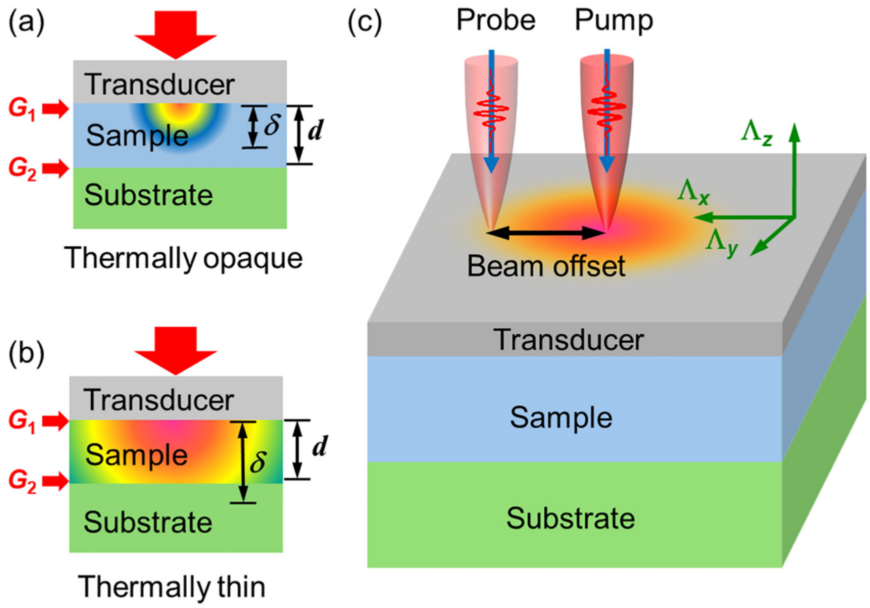

FIG. 2. The 2D schematics of the sample stack under the thermally opaque (a) and thermally thin (b) regimes, as determined by the film thickness (d) and thermal penetration depth (δ). (c) Schematic of the beam-offset approach. Λ_x, Λ_y, and Λ_z represent the thermal conductivity along the x, y, and z directions.

TABLE II. Summary of the transducers, measurement approaches, and corresponding conditions. The beam spot size was ∼12 μm for all through-plane measurements of Λ_z and ∼3 μm for all in-plane measurements of Λ_r.

Materials	Transducer	Λ_z measurements	Λ_r measurements
Alumina	Al	1.5, 9, and 18 MHz	N/A
Silica	Al		
AlN	Pt	9 and 18 MHz	Beam-offset, 1.5 MHz
Au	The thin film of interest	N/A	Routine TDTR, 1.5 MHz
Cu			Beam-offset, 1.5 MHz
$Ni_{80}Fe_{20}$		9 and 18 MHz	Beam-offset,1.5 MHz
$Co_{0.33}Fe_{0.67}$	Al	9 and 18 MHz	N/A

excitation has a penetration depth of $\delta = \sqrt{\Lambda_z/\pi f C}$, where Λ_z is the thermal conductivity, f is the modulation frequency, and C is the volumetric heat capacity of the sample, respectively. The thin-film sample is considered *thermally opaque* [Fig. 2(a)] when δ is less than the film thickness d, or *thermally thin* otherwise [Fig. 2(b)].[19] For the latter case, the measurement probes the second thermal interface (G_2), and the dual-frequency approach can be applied to improve the data reduction reliability.[15,19,25] For all measurements of Λ_z, a 5× objective lens was used to focus the pump and probe beams onto the samples' surface with a beam spot size of $w_0 \approx 12\,\mu$m ($1/e^2$ radius). The pump beam was modulated at 1.5, 9, or 18 MHz to optimize the measurement conditions based on our sensitivity analysis.

To probe in-plane thermal transport, we integrated the beam-offset approach with TDTR, where we varied the pump spot along the sample surface while keeping the probe spot fixed [Fig. 2(c)].[20–24,26,27] The out-of-phase signal (V_{out}) was measured at −50 ps as a function of the offset distance between the pump and probe beam spots. Λ_r was extracted by comparing the full width at half maximum (FWHM) of V_{out} to that of the model prediction. To measure Λ_r, the beam-offset approach was adopted in addition to routine TDTR, both of which were performed with a 20× objective lens ($w_0 \approx 3\,\mu$m) and at 1.5 MHz to ensure sufficient measurement sensitivity. Table II summarizes the detailed conditions for all through-plane and in-plane measurements.

For temperature-dependent thermal measurements, all samples were mounted using silver paint onto a temperature-controlled stage in an environmental chamber. The actual temperature of the samples was composed of three parts: the setting temperature (T_{set}), the steady-state temperature rise (ΔT_{ss}), and the per-pulse temperature rise (ΔT_{pp}).[15,19] The temperature correction procedures are detailed in our previous publications.[15,19]

IV. RESULTS AND DISCUSSION

A. Thermal properties of silica, alumina, and AlN as cladding materials/heat sink in HAMR

The out-of-plane thermal conductivities, Λ_z, of amorphous silica and amorphous alumina were measured at 1.5, 9, and 18 MHz from RT to 500 K. Extracting Λ_z over this temperature range requires the knowledge of several input parameters. The RT thermal conductivity of Al (Λ_{Al}) was converted from the electrical resistivity measured with the four-point probe method and the Wiedemann–Franz law. The T-dependent Λ_{Al} was determined based on the linear dependence of its electrical resistivity.[28] The volumetric heat capacity of each layer was taken from the literature.[29–32] The thicknesses of Al and silica ($d_{Al} = 64$ nm and $d_{SiO2} = 192$ nm) were determined from picosecond acoustics [Fig. 3(a)].[16–23,33] The thermal conductivity of Si was taken from the literature.[34] The measurements were insensitive to the interfacial thermal conductance of the Al/sample interface (G_1) due to the low thermal conductivity of the silica or alumina sample.

Figure 3(b) shows the representative TDTR ratio signals of the silica sample measured at RT, along with the best fits calculated using our 3D heat transfer model.[11,13–23] The 192 nm amorphous silica thin film has an RT thermal conductivity of 1.2 ± 0.08 W m^{-1} K^{-1}. Figure 3(c) compares the extracted T-dependent thermal conductivity of silica with some of the experimental data reported in the literature.[35–38] The extracted Λ_z of amorphous silica increases with temperature, a typical T dependence of Λ for amorphous solids. Over the studied temperature range, the extracted Λ_z of silica is slightly lower than that of the bulk,[35] but strongly consistent with the reported values of amorphous SiO_2 thin films of varying thicknesses, with an estimated uncertainty of 7%.[36–38] As reported by multiple experimental and computational studies, this consistency of Λ_z is expected due to its lack of thickness dependence in this thickness range.[39–46] In amorphous solids, the vibrational modes contributing to thermal transport are categorized as propagons (propagating, phonon-like), diffusons (non-propagating, delocalized), and locons (non-propagating, localized).[47–49] It is believed that thermal transport in SiO_2 is dominated by thickness-independent diffuson contributions, with minimal impact from the thickness-dependent propagon contributions.[39–46]

The RT Λ_z of the 1 μm alumina was measured to be 1.53 ± 0.19 W m^{-1} K^{-1}, and the corresponding T-dependent results from RT to 500 K are shown in Fig. 3(d), along with a comparison to the literature data.[50–54] Similar to the case of silica, Λ_z of alumina slightly increases with temperature due to its amorphous nature. With an estimated uncertainty of ∼13%, the measured Λ_z of the 1 μm alumina film agrees well with the literature-reported thermal conductivities within this temperature range.[50–54] It is noteworthy that the thermal conductivity of amorphous alumina can be significantly influenced by the material synthesis methods and the resulting atomic density.[53–56] For example, Lee *et al.* reported a 35% higher thermal conductivity for DC-sputtered amorphous alumina films compared to RF-sputtered films, despite only a ∼3% difference in density.[53] For films grown by atomic layer deposition (ALD), a 13% difference in atomic density can result in a 35% change in thermal conductivity.[55] In addition, no thickness dependence of amorphous alumina thermal conductivity has been observed in the range of 50 nm–5 μm.[51,55]

Λ_z and Λ_r of the polycrystalline AlN thin film were measured from RT to 500 K. As a non-metallic solid, thermal transport in AlN is dominated by phonons, with negligible contributions from electrons. Therefore, the microstructure and film thickness largely influence the thermal conductivity of AlN thin films due to

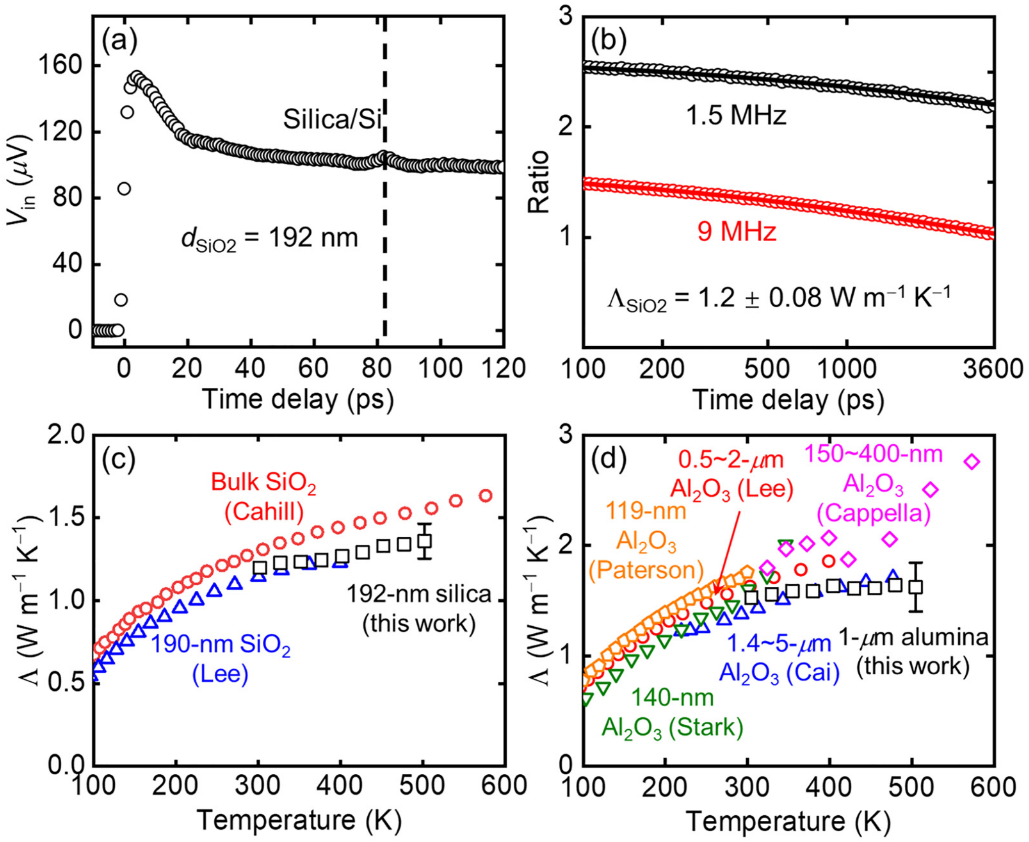

FIG. 3. (a) Representative picosecond acoustic signals in V_{in}, where the upward echo represents a round trip of the longitudinal acoustic wave traveling through the Al transducer and the silica film. (b) Representative TDTR ratio signals of silica measurements at 1.51 and 9 MHz at RT. The solid lines denote the best fits determined from simultaneous two-frequency fitting. (c) *T*-dependent Λ_z of the 192 nm silica (PECVD, black squares). For comparison, literature data are also presented for bulk fused silica (red circles)[35] and 190 nm silica (PECVD, blue triangles).[37] (d) *T*-dependent Λ_z of the 1 μm alumina (black squares), compared with literature-reported thermal conductivity of amorphous alumina with varying thicknesses: 140 nm (olive inverted triangles),[50] 1.4–5 μm (blue triangles),[51] 150–400 nm (pink diamonds),[52] 0.5–2 μm (red circles),[53] and 119 nm (orange pentagons).[54] Plots in (c) and (d) from Refs. 35, 37, and 54 are reproduced with permission from D. G. Cahill, Rev. Sci. Instrum. **61**(2), 802 (1990). Copyright 1990 AIP Publishing LLC; Lee *et al.*, J. Appl. Phys. **81**(6), 2590 (1997). Copyright 1997 AIP Publishing LLC; and Paterson *et al.*, J. Appl. Phys. **127**(24), 245105 (2020). Copyright 2020 AIP Publishing LLC. Plots in (c) and (d) from Refs. 50, 51, 52, and 53 are reproduced with permission from Stark *et al.*, Thin Solid Films **226**(1), 185 (1993). Copyright 1993 Elsevier; Cai *et al.*, J. Chem. Eng. Data. **55**(11), 4840 (2010). Copyright 2010 American Chemical Society; Cappella *et al.*, Adv. Eng. Mater. **15**(11), 1046 (2013). Copyright 2013 Wiley; and Lee *et al.*, Phys. Rev. B **52**(1), 253 (1995). Copyright 1995 American Physical Society.

phonon-boundary scattering.[9,57] The microstructural features of the AlN film were characterized using HAADF-STEM imaging. The film thickness (d_{AlN}) was measured to be 364 nm from the low-magnification cross-sectional HAADF-STEM image, as shown in Fig. 4(a). Grain boundaries in the AlN film appear as bright lines due to contrast differences, and these boundaries are identified as sharp peaks in the corresponding HAADF intensity linescan. Statistical analysis of the intensity linescan indicates an average grain size of 30 nm, ranging from 17 to 45 nm. High-resolution HAADF-STEM imaging resolves individual grains, as shown in Fig. 4(b). An atomic-resolution HAADF-STEM image further reveals the uniform crystal structure of the grains.

For through-plane Λ_z measurements, two modulation frequencies of 9 and 18 MHz, and the 5× objective lens ($w_0 \approx 12\,\mu$m), were used. For in-plane Λ_r measurements, the beam-offset approach with a 20× objective lens ($w_0 \approx 3\,\mu$m) at 1.5 MHz was used (Table II).[20–24,26] For data reduction, the thermal conductivity of the Pt transducer (Λ_{Pt}) was obtained using the same approach for the Al transducer,[58,59] and the thermal conductivity of Si was taken from the literature.[34] The volumetric heat capacity of each layer was taken from the literature.[30,60,61] The thickness of the Pt transducer ($d_{Pt} = 77$ nm) was measured using picosecond acoustics for a Pt/SiO$_2$ (300)/Si control sample in the same batch. The Λ_z measurements from RT to 500 K are in the "*thermally thin*" regime, given the high thermal conductivity of the polycrystalline AlN films compared to amorphous silica or alumina. In this case, G_2 is sensitive, and dual-frequency TDTR was applied to reliably determine G_2, and thereby improving the measurement accuracy of

Λ_z.[15,19,25] At each temperature, Λ_z and G_1 were determined from through-plane measurements and then served as input parameters to extract Λ_r via the beam-offset approach. The assumption of frequency-independent thermal conductivity is required when applying dual-frequency TDTR,[62] and no apparent frequency dependence of the AlN thermal conductivity was observed in this work.

The representative TDTR ratio signals from the through-plane measurements and the out-of-phase (V_{out}) signals from the in-plane beam-offset measurements are shown in Figs. 4(c) and 4(d), with Λ_z and Λ_r being 42 ± 6.1 and 58 ± 14.7 W $\text{m}^{-1}\,\text{K}^{-1}$ at RT, respectively. Compared to a bulk single crystal with an isotropic thermal conductivity of ∼330 W $\text{m}^{-1}\,\text{K}^{-1}$, the AlN thin film exhibits significantly lower thermal conductivities.[5–10] The comparison of the extracted Λ_z and Λ_r of polycrystalline AlN with the previous measurements of sputtered AlN films is illustrated in Fig. 4(e).[9,57] The reduced Λ_z of AlN thin films can be attributed to phonon-boundary scattering and phonon-point defect scattering,[57] which is known to have homogeneous impacts on both Λ_z and Λ_r.[63–65] In addition, Λ_r is primarily influenced by the film microstructure.[9] The polycrystalline AlN film is composed of columnar grains aligned perpendicular to the substrate. The extracted Λ_r corresponds to an averaged lateral (in-plane) grain size of 35 nm [Fig. 4(e)],[9] consistent with the estimate obtained through the HAADF intensity linescan [Fig. 4(a)]. The films from prior studies with lower Λ_r values had an averaged lateral grain size of ∼20 nm,[9] further suggesting that in-plane thermal transport in polycrystalline AlN films with columnar textures is limited by phonon-grain boundary scattering. The high-T performance of polycrystalline AlN from RT to 500 K is examined by plotting the T-dependent Λ_z and Λ_r in Fig. 4(f). The uncertainties, averaged over the measurement temperature range, are ∼15% for Λ_z and ∼30% for Λ_r. Λ_z and Λ_r decrease with temperature, reducing to 20–30 W $\text{m}^{-1}\,\text{K}^{-1}$ at 500 K.

B. Thermal properties of Au and Cu films for heat sinks and electromagnet coils in HAMR

The in-plane thermal conductivities of a 50 nm Au and a 100 nm Cu film were measured using TDTR from RT to 500 K. Thermal transport in both metals is primarily driven by free electrons. Λ_r of the 46 nm Au film was measured using routine TDTR with the 20× objective lens ($w_0 \approx 3\,\mu$m) at 1.51 MHz by treating the Au film as the transducer on a reference SiO_2/Si sample. For data reduction, the volumetric heat capacities of Au, Cr, SiO_2, and Si and the thermal conductivity of Si are taken from the literature.[30,31,34] The thicknesses of the Au film ($d_{\text{Au}} = 46.1$ nm) and SiO_2 ($d_{\text{SiO2}} = 287.8$ nm) were determined from SEM. The thermal interfaces of Au/Cr, Cr/SiO_2, and the 5 nm film of Cr were lumped as an effective interfacial thermal conductance "G_1" [see Fig. 5(a)], the only fitting parameter in addition to Λ_r.

The representative TDTR ratio signal and its best fit for the Au film at RT are plotted in Fig. 5(b). The extracted Λ_r is 216 W $\text{m}^{-1}\,\text{K}^{-1}$ with an estimated uncertainty of 24%, reasonably matching the result from the four-point probe measurement at RT (234 W $\text{m}^{-1}\,\text{K}^{-1}$). This measured Λ_r is ∼32% lower than the bulk thermal conductivity of Au reported in the literature (317 W $\text{m}^{-1}\,\text{K}^{-1}$).[66] Extensive theoretical and experimental studies indicate that, unlike bulk materials, thermal transport in metallic thin films is affected by grain boundary and surface boundary scattering.[66–77] For the 46 nm Au film, diffuse electron-boundary scattering plays a substantial role in thermal transport as the characteristic dimension of the film (e.g., film thickness or grain size) becomes comparable to the electron MFPs, leading to a reduced thermal conductivity.[66–76] To better quantify this impact, a model proposed by Qiu and Tien based on Mayadas's theory is applied,[67,71]

$$\frac{\Lambda_{\text{f}}}{\Lambda_{\text{b}}} = \left[1 + \frac{3}{8\delta}(1 - P) + \frac{7}{5}\alpha\right]^{-1}, \tag{1}$$

where

$$\alpha = \frac{\text{MFP}}{D}\frac{R}{1 - R}. \tag{2}$$

In this model, Λ_{b} and Λ_{f} are the bulk and thin-film thermal conductivities, respectively. δ is the ratio of the film thickness d to the electron MFP. P and R are the specular reflection coefficients of electrons at film surfaces and the grain-boundary reflection coefficients of electrons, respectively. D stands for the averaged lateral grain size of the film.

Using this model, the RT thermal conductivity ratio of $\Lambda_{\text{f}}/\Lambda_{\text{b}}$ is calculated as a function of δ and compared to the experimental results in Fig. 5(c).[72] As input parameters, an electron MFP of 42 nm and P of 0.5 for Au are taken from the literature.[66–69,78] The averaged lateral grain size D is taken as the film thickness (46.1 nm) as a first approximation.[66,70–73] Four cases are calculated with R varied from 0 to 0.3 and compared to the experimental results, as shown in Fig. 5(c), where Λ_{f} monotonically decreases with R, reflecting the effect of electron-grain boundary scattering. The comparison suggests that the 46.1 nm Au film in this study has an R value of ∼0.2, falling within the literature range of 0.17–0.35.[72–75] Figure 5(d) depicts Λ_r measured from RT to 500 K for the Au film, with an average uncertainty of ∼25%. There is no observable T dependence of Λ_r in this temperature range, consistent with the theoretical and experimental studies in the literature.[79]

Λ_r of the 100 nm Cu film was measured with the beam-offset approach using the 20× objective lens and at 1.51 MHz by using the copper thin film as the transducer.[20–24,26] As with the Au film sample, the volumetric heat capacities of individual layers in the Cu film sample were taken from the literature,[30,31,34] and the thicknesses of Cu ($d_{\text{Cu}} = 101.3$ nm) and SiO_2 ($d_{\text{SiO2}} = 357.5$ nm) were determined from SEM. The effective interfacial thermal conductance of G_1 combines the thermal interfaces of Cu/Cr, Cr/SiO_2, and the 5 nm Cr film. With the beam-offset approach, thermal measurements are not sensitive to G_1.

Figure 6(a) displays the out-of-phase (V_{out}) signals from the beam-offset measurements at RT. The V_{out} FWHM of 9.80 μm corresponds to a Λ_r of 276 W $\text{m}^{-1}\,\text{K}^{-1}$ with an uncertainty of 7%, aligning well with the RT result from four-point probe measurements (279 W $\text{m}^{-1}\,\text{K}^{-1}$). Similar to the Au film in this work, Λ_r of the Cu film is ∼30% lower than the bulk value (400 W $\text{m}^{-1}\,\text{K}^{-1}$).[66] Using the same model proposed by Qiu and Tien, the averaged lateral grain size in the Cu film is 43 nm, as shown in Fig. 6(b).[66,70,71,76] Measurements of the Cu film from RT to 500 K also suggest no

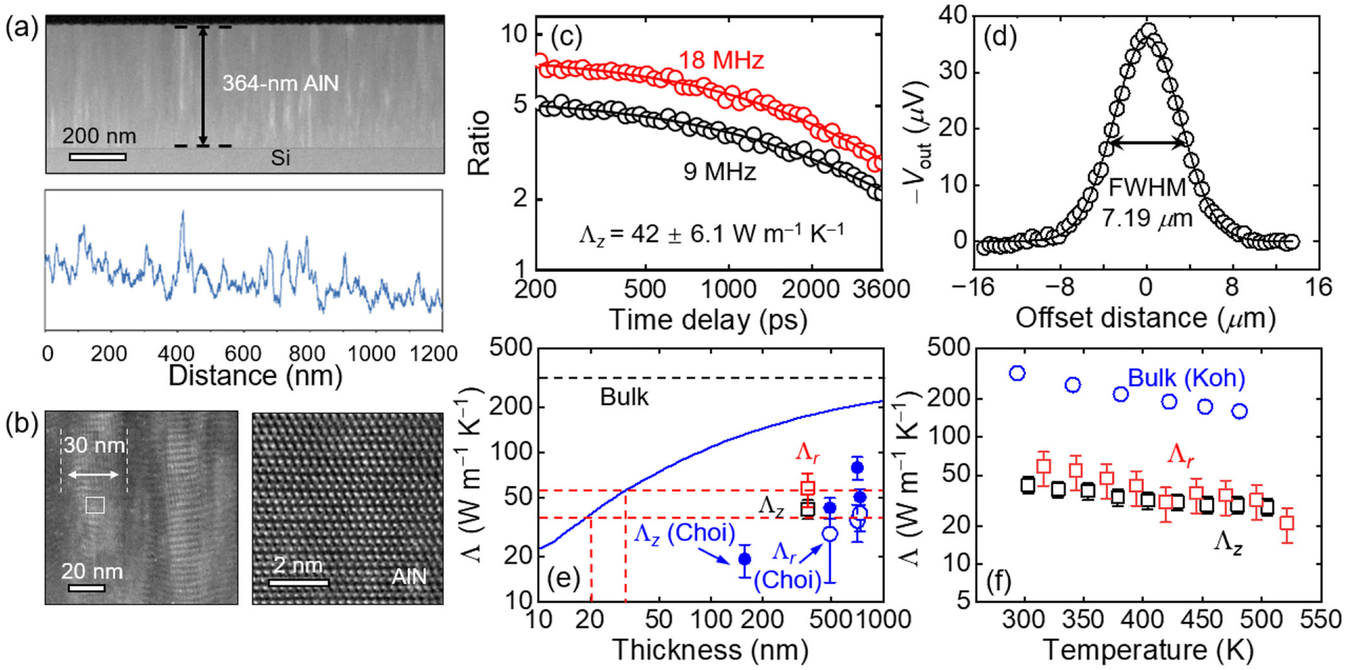

FIG. 4. (a) A low-magnification HAADF-STEM image of the polycrystalline AlN film grown on the [001] Si substrate. Here, grain boundaries appear as bright lines. The HAADF intensity linescan below the image shows the grain boundaries as sharp peaks. (b) The high-resolution HAADF-STEM image shows a few such grains, each about 30 nm in size (left). The atomic-resolution HAADF-STEM image (from the box in the left panel) shows the crystalline structure of a single AlN grain (right). (c) Representative TDTR ratio signal at 9 (black) and 18 (red) MHz at RT. The solid lines denote the best fits determined from simultaneous two-frequency fitting. (d) Representative V_{out} signals from the beam-offset approach at RT. (e) The comparison of the extracted Λ_z and Λ_r (open squares) with literature-reported values of sputtered AlN films (blue circles) as a function of film thickness.[9] Compared to the model prediction (blue line),[57] the Λ_r values in this work (red square) and the previous study (red circles) correspond to a lateral grain size of 35 and 20 nm, respectively. (f) *T*-dependent Λ_z (black squares) and Λ_r (red squares) from RT to 500 K. The uncertainties are ∼15% and 30% for Λ_z and Λ_r, respectively, as averaged over the measurement temperature range. The *T*-dependent thermal conductivity of a 22 μm thick AlN single crystal from the literature is plotted for comparison (blue circles).[10] Plots in (e) from Refs. 9 and 57 are reproduced with permission from Song *et al.*, J. Appl. Phys. **132**(17), 175108 (2022). Copyright 2022 AIP Publishing LLC; and Xu *et al.*, J. Appl. Phys. **126**(18), 185105 (2019). Copyright 2019 AIP Publishing LLC. Plots in (f) from Ref. 10 are reproduced with permission from Koh *et al.*, ACS Appl. Mater. Interfaces **12**(26), 29443 (2020). Copyright 2020 American Chemical Society.

observable *T* dependence for Λ_r [Fig. 6(c)], similar to the case of the Au film.

C. Thermal properties of CoFe and NiFe for write poles and magnetic shields in HAMR

The through-plane Λ_z of the 300 nm $Co_{0.33}Fe_{0.67}$ film was measured using TDTR with the 5× objective lens ($w_0 \approx 12\,\mu$m) at 9 and 18 MHz from RT to 500 K. Similar to the measurements of dielectric materials, Al was used as the transducer, and its thermal conductivity was determined from the electrical measurements of an Al/SiO$_2$/Si reference sample. The thermal conductivity of the Cu layer and Si were taken from the literature.[34,70] The volumetric heat capacity of the CoFe film was estimated from the heat capacities of Co and Fe based on stoichiometry.[30] The volumetric heat capacities of other layers were taken from the literature.[29–31] The thickness of Al (d_{Al} = 64 nm) was determined from picosecond acoustics, and the thicknesses of other individual layers were determined from SEM measurements (Table I).[16–23,33] Due to the challenge in separating the 300 nm electroplated CoFe film and the 30 nm sputtered CoFe film in TDTR analysis, Λ_z of CoFe was taken as the effective thermal conductivity of the two combined CoFe layers [Fig. 7(a)]. The *G* values of the CoFe/Cu and Cu/Cr interfaces were set to 3.7 GW m^{-2} K^{-1}, a typical value for metal–metal interfaces found in the literature.[80] The electronic contribution to Λ_z of CoFe at RT was estimated from the four-point probe measurements using a parallel-resistance model incorporating the lumped resistances of the CoFe, Cu, and Cr films, with literature values used for Cu and Cr resistivities.[70,81]

Figure 7(b) shows the representative ratio signals at 9 and 18 MHz collected at RT and the corresponding best fits, resulting in a value of 31.9 ± 12.2 W m^{-1}K^{-1} for Λ_z of CoFe. Using the parallel-resistance model, the estimated electronic thermal conductivity is 23.6 W m^{-1} K^{-1}, suggesting a ratio of ∼3:1 for the electronic vs phononic contributions to thermal transport in CoFe. The *T*-dependent thermal conductivity of CoFe is plotted in Fig. 7(c), along with the experimental data reported in the literature.[82] For 60–80 nm thick CoFe films, the thermal conductivity gradually increases with *T* below ∼200 K before plateauing.[82] For temperatures above 200 K, Λ of CoFe appears temperature independent, consistent

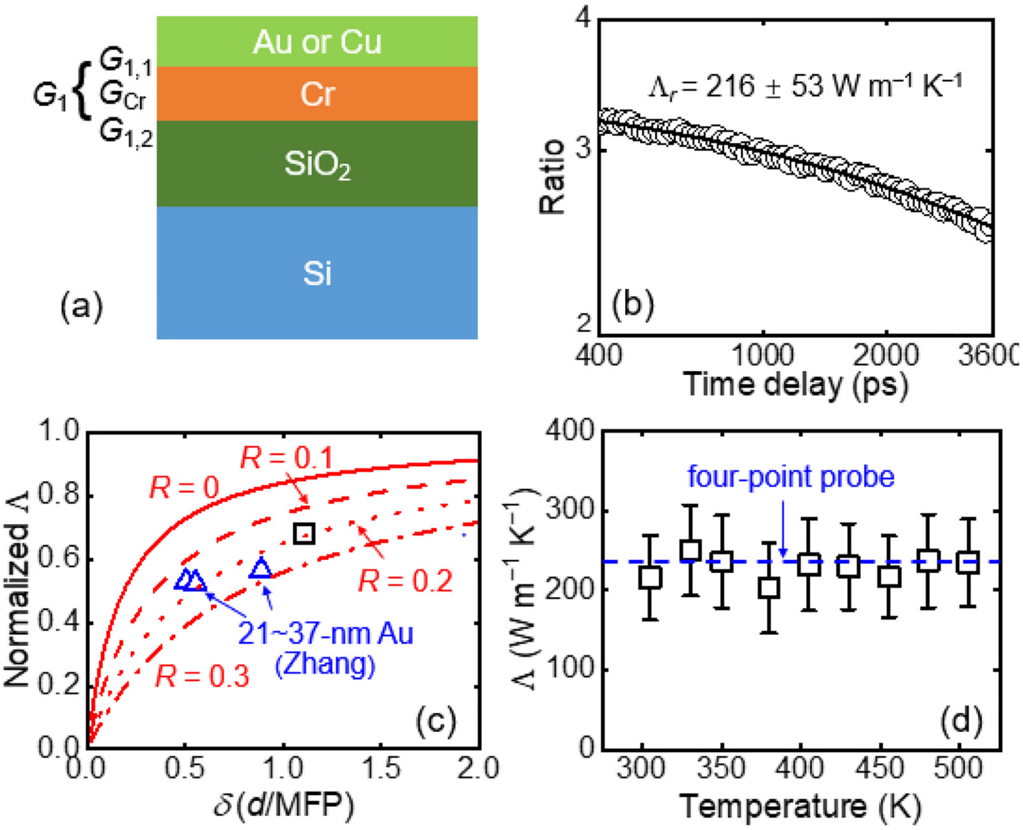

FIG. 5. (a) The sample schematic. G_1 is the effective interfacial thermal conductance combining the thermal interfaces of Au (or Cu)/Cr ($G_{1,1}$), Cr/SiO$_2$ ($G_{1,2}$), and the 5 nm Cr film. (b) Representative TDTR ratio signal at 1.51 MHz at RT. The solid line denotes the best fit. (c) The calculated ratio of Λ_f/Λ_b vs δ at RT using the model proposed by Qiu and Tien in comparison with the experimental results of this work (black square) and from the literature (blue triangles).[72] The value of R is set as 0 (red solid line), 0.1 (red dashed line), 0.2 (red dotted line), and 0.3 (red dashed-dotted line) to illustrate the impact of grain boundary scattering on thermal conductivity. (d) Λ_r of the Au film from RT to 500 K. The blue dashed line denotes the electronic thermal conductivity converted from the four-point probe measurements at RT. Plots in (c) from Ref. 72 are reproduced with permission from Zhang *et al.*, Phys. Rev. B **74**(13), 134109 (2006). Copyright 2006 American Physical Society.

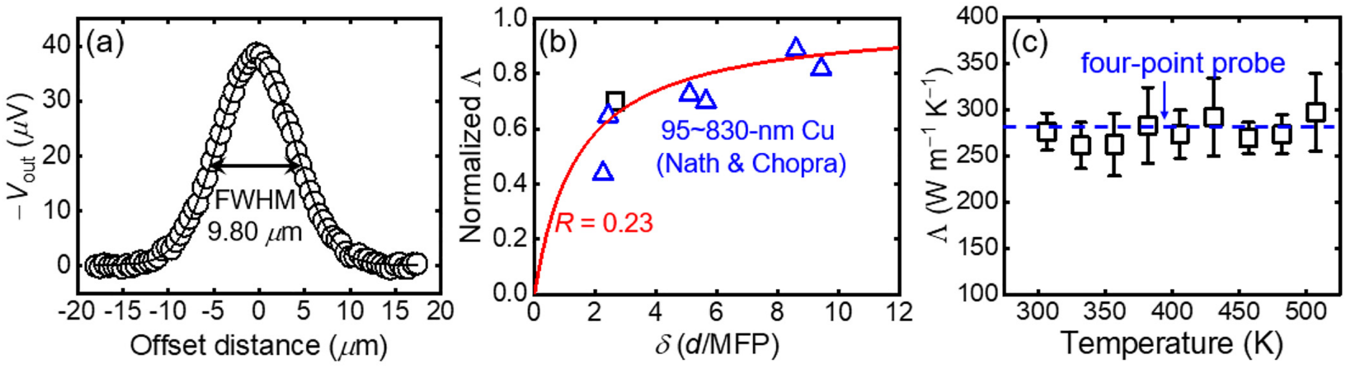

FIG. 6. (a) Representative V_{out} signals from the beam-offset measurements at RT. (b) The calculated ratio of Λ_f/Λ_b of Cu (red solid line) vs δ at RT using the model proposed by Qiu and Tien in comparison with the experimental results of this work (black square) and from the literature (blue triangles).[70] (c) Λ_r of the Cu film from RT to 500 K. The blue dashed line denotes the electronic thermal conductivity converted from four-point probe measurements at RT. Plots in (b) from Ref. 70 are reproduced with permission from Nath *et al.*, Thin Solid Films **20**(1), 53 (1974). Copyright 1974 Elsevier.

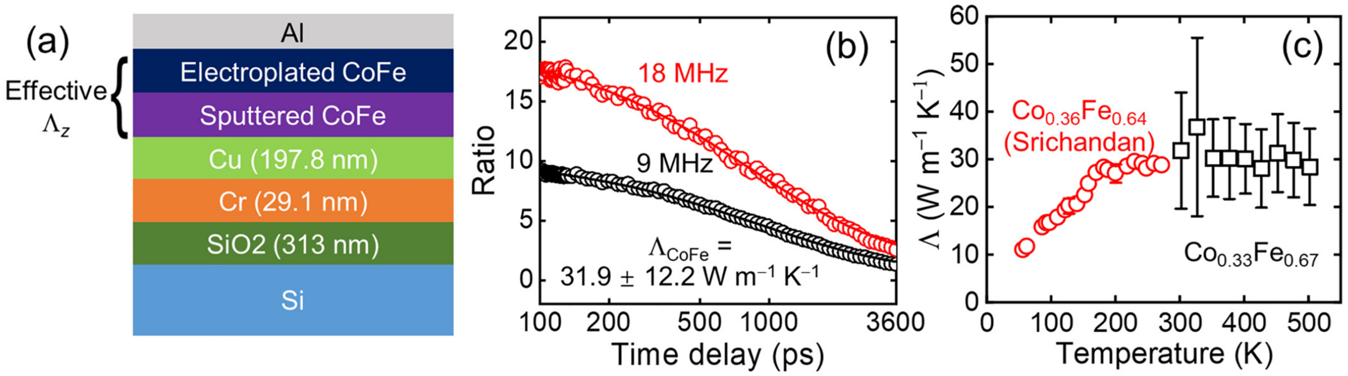

FIG. 7. (a) The sample schematic for measuring Λ_z taken as the effective thermal conductivity of the combined CoFe layers. (b) Representative TDTR signals from RT measurements of the CoFe sample at 9 (black) and 18 (red) MHz. The solid lines denote the best fit from the two-frequency fitting. (c) *T*-dependent through-plane thermal conductivity of the CoFe film (black squares). Literature data of 60–80 nm $Co_{0.36}Fe_{0.64}$ films (red circles) are also plotted for comparison.[82] Plots in (c) from Ref. 82 are reproduced with permission from Srichandan *et al.*, Phys. Rev. B **98**(2), 020406 (2018). Copyright 2018 American Physical Society.

with the results of this work for $300\,K < T < 500\,K$.[82] The flat Λ observed at higher temperatures is expected for an alloy with electrons as dominant heat carriers. A literature study indicated that $Co_{0.36}Fe_{0.64}$ films possess a mixed body-centered cubic (bcc) and a face-centered cubic (fcc) phase, while films with lower Co content tend to adopt a single bcc phase.[82] In such disordered polycrystalline systems, electron MFPs are expected to be on the atomic scale, significantly suppressing size effects on the electronic contribution to thermal transport.[82] Hence, there is little difference in the thermal conductivity of the 60–80 nm CoFe films in literature and 330 nm CoFe film in this work.

The through-plane Λ_z and in-plane Λ_r of the 100 nm $Ni_{80}Fe_{20}$ film were measured from RT to 500 K using routine TDTR ($w_0 \approx 12\,\mu m$, 9 and 18 MHz) and the beam-offset approach ($w_0 \approx 3\,\mu m$, 1.51 MHz), respectively. In both routine TDTR and beam-offset measurements, the $Ni_{80}Fe_{20}$ thin film served as the transducer. Four-point probe measurements were also conducted to cross-check the in-plane Λ_r at RT. The data reduction for NiFe was similar to that for the Au and Cu films. The interfacial thermal conductance of the NiFe/SiO_2 interface (G_1) and Λ_z of NiFe were the two fitting parameters used in our routine TDTR measurements. The modulation frequency of 18 MHz, which offers a higher sensitivity to G_1, was used to extract G_1, and Λ_z was determined exclusively at 9 MHz before it served as an input parameter to extract Λ_r from the beam-offset measurements at 1.51 MHz.

The representative ratio signals from routine TDTR measurements of Λ_z and the V_{out} signals from beam-offset measurements are plotted in Figs. 8(a) and 8(b). The extracted Λ_z and Λ_r at RT

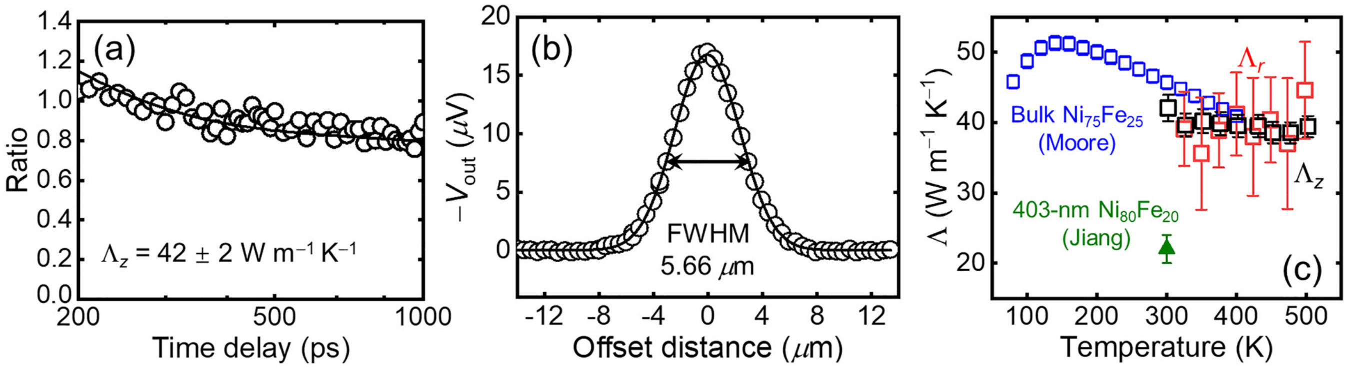

FIG. 8. (a) Representative signals from the routine TDTR measurements of the NiFe sample at 9 MHz and the corresponding best fit. (b) Representative V_{out} signals from the in-plane beam-offset measurements at RT. The NiFe film is treated as the transducer in both measurements. (c) *T*-dependent Λ_z (black squares) and Λ_r (red squares) of the NiFe film in comparison with the experimental data reported in previous studies for bulk $Ni_{75}Fe_{25}$ (blue diamonds) and a 403 nm $Ni_{80}Fe_{20}$ film (green triangle).[25,85] Plots in (c) from Refs. 25 and 85 are reproduced with permission from Jiang *et al.*, Rev. Sci. Instrum. **87**(7), 075101 (2016). Copyright 2016 AIP Publishing LLC; and Moore *et al.*, J. Appl. Phys. **42**(8), 3114 (1971). Copyright 1971 AIP Publishing LLC.

were 42 ± 2 and $39 \pm 5.3\,\mathrm{W\,m^{-1}\,K^{-1}}$, respectively, indicating that thermal transport in the NiFe alloy film exhibits little anisotropy and is unlikely to be influenced by electron-boundary scattering due to the shorter electron MFPs (~10 nm)[25] compared with the film thickness (~100 nm). Using a Lorenz number of $2.38 \times 10^{-8}\,\mathrm{W\,\Omega\,K^{-2}}$ from the literature,[83,84] the electronic thermal conductivity converted from four-point probe measurements was $34.2\,\mathrm{W\,m^{-1}\,K^{-1}}$. The difference between the total and electronic thermal conductivities of NiFe is attributed to phonon contributions, which, while minor compared to electronic contributions, can account for $2–5\,\mathrm{W\,m^{-1}\,K^{-1}}$ to the thermal conductivity of metallic alloys, as reported in previous studies.[25,85,86]

The T-dependent Λ_z and Λ_r are shown in Fig. 8(c) in comparison with the experimental data from the literature. Moore reported similar values of thermal conductivity for bulk $\mathrm{Ni_{75}Fe_{25}}$ from RT to 400 K, similar to our results for the 100 nm $\mathrm{Ni_{80}Fe_{20}}$ film, whereas Jiang measured a much lower thermal conductivity of $22 \pm 2\,\mathrm{W\,m^{-1}\,K^{-1}}$ for a 403 nm $\mathrm{Ni_{80}Fe_{20}}$ thin film at RT.[25,85] The discrepancy can be attributed to the differences in the electrical resistivity.[25,85] Moore measured an electrical resistivity of $15.98\,\mu\Omega\,\mathrm{cm}$ for bulk $\mathrm{Ni_{75}Fe_{25}}$, while Jiang reported a resistivity of $32.3\,\mu\Omega\,\mathrm{cm}$ for the $\mathrm{Ni_{80}Fe_{20}}$ film at RT, leading to a difference in thermal conductivities.[25,85]

V. CONCLUSIONS

This work investigates the thermal properties of dielectric, metallic, and alloy materials used in HAMR applications over a temperature range from RT to 500 K. The thermal conductivities of the amorphous silica and alumina films align well with the literature values, exhibiting a gradual increase with temperature. The weak thickness dependence of thermal conductivity is attributed to the dominant diffuson contribution to thermal transport. Compared to bulk single crystals, the polycrystalline AlN thin film has significantly lower thermal conductivity in both through-plane and in-plane directions, partially due to phonon-boundary and phonon-point defect scattering. Both in-plane and through-plane thermal conductivities of AlN decrease from $40–60\,\mathrm{W\,m^{-1}\,K^{-1}}$ at RT to $20–30\,\mathrm{W\,m^{-1}\,K^{-1}}$ at 500 K. The 50 nm Au film and the 100 nm Cu film also show reduced thermal conductivities compared to their bulk counterparts, primarily due to diffuse electron-boundary scattering. Using an empirical model, the grain sizes of both films are estimated as 45 nm, comparable to the electron MFPs at RT. The thermal conductivities of both metallic films are independent of temperature from RT to 500 K, a trend similar to that observed for the CoFe and NiFe alloy films. Electrons dominate thermal transport in both CoFe and NiFe alloy films, while phonons can also make a substantial contribution to the thermal conductivity of the alloys. This work provides valuable experimental data on the thermal properties of HAMR materials over a typical operating temperature range. The results will not only enhance the understanding of thermal transport mechanisms in these technologically important materials but also directly support the design and optimization of HAMR devices in the data-storage industry.

ACKNOWLEDGMENTS

This work was primarily supported by the National Science Foundation (NSF, No. CBET-2226579). Xiaotian Xu and Chi Zhang also thank the partial support from the NSF through the MRSEC program (NSF, No. DMR-2011401). Portions of this work were conducted in the Minnesota Nano Center, supported by the NSF through the National Nanotechnology Coordinated Infrastructure under No. ECCS-2025124. Sample fabrication and other project activities at Seagate were supported by Joseph Roth, Jie Gong, Steve Riemer, Phillip Huang, Duy Tran, Tong Zhao, Eric Singleton, Neil Zuckerman, and Xuan Zheng.

AUTHOR DECLARATIONS

Conflict of Interest

The authors declare no conflict of interest.

Author Contributions

Xiaotian Xu: Data curation (equal); Formal analysis (equal); Methodology (equal); Writing – original draft (equal); Writing – review & editing (supporting). **Chi Zhang:** Data curation (equal); Formal analysis (equal); Methodology (equal); Supervision (supporting); Writing – original draft (equal); Writing – review & editing (equal). **Silu Guo:** Data curation (supporting); Formal analysis (supporting); Methodology (supporting); Writing – original draft (supporting); Writing – review & editing (supporting). **Nicholas C. A. Seaton:** Data curation (supporting); Formal analysis (supporting); Methodology (supporting); Writing – review & editing (supporting). **K. Andre Mkhoyan:** Project administration (supporting); Supervision (supporting); Writing – original draft (supporting); Writing – review & editing (supporting). **Joseph Roth:** Methodology (supporting); Writing – review & editing (supporting). **Jie Gong:** Methodology (supporting); Writing – review & editing (supporting). **Xuan Zheng:** Funding acquisition (supporting); Methodology (supporting); Writing – review & editing (supporting). **Neil Zuckerman:** Conceptualization (equal); Funding acquisition (supporting); Methodology (supporting); Writing – original draft (supporting); Writing – review & editing (supporting). **Xiaojia Wang:** Conceptualization (equal); Funding acquisition (lead); Project administration (lead); Supervision (lead); Writing – original draft (supporting); Writing – review & editing (equal).

DATA AVAILABILITY

The data that support the findings of this study are available from the corresponding authors upon reasonable request.

REFERENCES

[1] H. Ho, A. A. Sharma, W.-L. Ong, J. A. Malen, J. A. Bain, and J.-G. Zhu, Appl. Phys. Lett. **103**(13), 131907 (2013).
[2] M. T. Kief and R. H. Victora, MRS Bull. **43**(2), 87 (2018).
[3] D. Weller, G. Parker, O. Mosendz, A. Lyberatos, D. Mitin, N. Y. Safonova, and M. Albrecht, J. Vac. Sci. Technol. B **34**(6), 060801 (2016).
[4] E. A. Dobisz, Z. Z. Bandic, T.-W. Wu, and T. Albrecht, Proc. IEEE **96(11)**, 1836 (2008).
[5] G. A. Slack, J. Phys. Chem. Solids **34**(2), 321 (1973).
[6] G. A. Slack, R. A. Tanzilli, R. O. Pohl, and J. W. Vandersande, J. Phys. Chem. Solids **48**(7), 641 (1987).

[7]R. Rounds, B. Sarkar, D. Alden, Q. Guo, A. Klump, C. Hartmann, T. Nagashima, R. Kirste, A. Franke, M. Bickermann, Y. Kumagai, Z. Sitar, and C. Ramon, J. Appl. Phys. **123**(18), 185107 (2018).
[8]A. V. Inyushkin, A. N. Taldenkov, D. A. Chernodubov, E. N. Mokhov, S. S. Nagalyuk, V. G. Ralchenko, and A. A. Khomich, J. Appl. Phys. **127**(20), 205109 (2020).
[9]Y. Song, C. Zhang, J. S. Lundh, H.-L. Huang, Y. Zheng, Y. Zhang, M. Park, T. Mirabito, R. Beaucejour, C. Chae, N. McIlwaine, G. Esteves, T. E. Beechem, C. Moe, R. Dargis, J. Jones, J. H. Leach, R. Lavelle, D. W. Snyder, J.-P. Maria, R. H. Olsson, J. M. Redwing, A. Ansari, J. Hwang, X. Wang, B. M. Foley, S. E. Trolier-McKinstry, and S. Choi, J. Appl. Phys. **132**(17), 175108 (2022).
[10]Y. R. Koh, Z. Cheng, A. Mamun, M. S. Bin Hoque, Z. Liu, T. Bai, K. Hussain, M. E. Liao, R. Li, J. T. Gaskins, A. Giri, J. Tomko, J. L. Braun, M. Gaevski, E. Lee, L. Yates, M. S. Goorsky, T. Luo, A. Khan, S. Graham, and P. E. Hopkins, ACS Appl. Mater. Interfaces **12**(26), 29443 (2020).
[11]J. Zhu, X. Wu, D. M. Lattery, W. Zheng, and X. Wang, Nanoscale Microscale Thermophys. Eng. **21**(3), 177 (2017).
[12]Y. Wang, J. Y. Park, Y. K. Koh, and D. G. Cahill, J. Appl. Phys. **108**(4), 043507 (2010).
[13]D. G. Cahill, MRS Bull. **43**(10), 782 (2018).
[14]D. G. Cahill, Rev. Sci. Instrum. **75**(12), 5119 (2004).
[15]Y. Zhang, W. M. Postiglione, R. Xie, C. Zhang, H. Zhou, V. Chaturvedi, K. Heltemes, H. Zhou, T. Feng, C. Leighton, and X. Wang, Nat. Commun. **14**(1), 2626 (2023).
[16]X. Wu, J. Walter, T. Feng, J. Zhu, H. Zheng, J. F. Mitchell, N. Biškup, M. Varela, X. Ruan, C. Leighton, and X. Wang, Adv. Funct. Mater. **27**(47), 1704233 (2017).
[17]X. Wu, B. L. Greenberg, Y. Zhang, J. T. Held, D. Huang, J. G. Barriocanal, K. A. Mkhoyan, E. S. Aydil, U. Kortshagen, and X. Wang, Phys. Rev. Mater. **4**(8), 086001 (2020).
[18]Y. Zhang, M. A. Eslamisaray, T. Feng, U. Kortshagen, and X. Wang, Nanoscale Adv. **4**(1), 87 (2021).
[19]C. Zhang, F. Liu, S. Guo, Y. Zhang, X. Xu, K. A. Mkhoyan, B. Jalan, and X. Wang, Appl. Phys. Lett. **123**(4), 042201 (2023).
[20]J. Zhu, H. Park, J. Y. Chen, X. Gu, H. Zhang, S. Karthikeyan, N. Wendel, S. A. Campbell, M. Dawber, X. Du, M. Li, J.-P. Wang, R. Yang, and X. Wang, Adv. Electron. Mater. **2**(5), 1600040 (2016).
[21]Y. Zhang, Q. Su, J. Zhu, S. Koirala, S. J. Koester, and X. Wang, Appl. Phys. Lett. **116**(20), 202101 (2020).
[22]J. Zhu, T. Feng, S. Mills, P. Wang, X. Wu, L. Zhang, S. T. Pantelides, X. Du, and X. Wang, ACS Appl. Mater. Interfaces **10**(47), 40740 (2018).
[23]T. Feng, X. Wu, X. Yang, P. Wang, L. Zhang, X. Du, X. Wang, and S. T. Pantelides, Adv. Funct. Mater. **30**(5), 1907286 (2020).
[24]J. P. Feser, J. Liu, and D. G. Cahill, Rev. Sci. Instrum. **85**(10), 104903 (2014).
[25]P. Jiang, B. Huang, and Y. K. Koh, Rev. Sci. Instrum. **87**(7), 075101 (2016).
[26]J. P. Feser and D. G. Cahill, Rev. Sci. Instrum. **83**(10), 104901 (2012).
[27]X. J. Wang, T. Mori, I. Kuzmych-Ianchuk, Y. Michiue, K. Yubuta, T. Shishido, Y. Grin, S. Okada, and D. G. Cahill, APL Mater. **2**(4), 046113 (2014).
[28]P. D. Desai, H. M. James, and C. Y. Ho, J. Phys. Chem. Ref. Data **13**(4), 1131 (1984).
[29]D. A. Ditmars, C. A. Plint, and R. C. Shukla, Int. J. Thermophys. **6**(5), 499 (1985).
[30]Y. Touloukian and E. Buyco, *Thermophysical Properties of Matter-the TPRC Data Series. Volume 4. Specific Heat-Metallic Elements and Alloys* (Thermophysical and Electronic Properties Information Analysis Center, 1971).
[31]Y. Touloukian and E. Buyco, *Thermophysical Properties of Matter-The TPRC Data Series. Volume 5. Specific Heat-Nonmetallic Solids* (Thermophysical and Electronic Properties Information Analysis Center, 1970).
[32]G. T. Furukawa, T. B. Douglas, R. E. McCoskey, and D. C. Ginnings, J. Res. Nat. Bureau Stand. **57**(2), 67 (1956).
[33]G. T. Hohensee, W.-P. Hsieh, M. D. Losego, and D. G. Cahill, Rev. Sci. Instrum. **83**(11), 114902 (2012).
[34]H. R. Shanks, P. D. Maycock, P. H. Sidles, and G. C. Danielson, Phys. Rev. **130**(5), 1743 (1963).
[35]D. G. Cahill, Rev. Sci. Instrum. **61**(2), 802 (1990).
[36]M. B. Kleiner, S. A. Kuhn, and W. Weber, IEEE Trans. Electron Devices **43**(9), 1602 (1996).
[37]S.-M. Lee and D. G. Cahill, J. Appl. Phys. **81**(6), 2590 (1997).
[38]D.-J. Yao, W.-C. Lai, and H.-C. Chien, "Temperature dependence of thermal conductivity for silicon dioxide," in *International Conference on Micro/Nanoscale Heat Transfer*, Tainan, Taiwan, *6–9 June 2018*, (ASME, 2008), p. 435.
[39]T. Yamane, N. Nagai, S.-I. Katayama, and M. Todoki, J. Appl. Phys. **91**(12), 9772 (2002).
[40]K. T. Regner, D. P. Sellan, Z. Su, C. H. Amon, A. J. McGaughey, and J. A. Malen, Nat. Commun. **4**(1), 1640 (2013).
[41]Y. Hu, L. Zeng, A. J. Minnich, M. S. Dresselhaus, and G. Chen, Nat. Nanotechnol. **10**(8), 701 (2015).
[42]J. L. Braun, C. H. Baker, A. Giri, M. Elahi, K. Artyushkova, T. E. Beechem, P. M. Norris, Z. C. Leseman, J. T. Gaskins, and P. E. Hopkins, Phys. Rev. B **93**(14), 140201 (2016).
[43]L. Yang, Q. Zhang, Z. Cui, M. Gerboth, Y. Zhao, T. T. Xu, D. G. Walker, and D. Li, Nano Lett. **17**(12), 7218 (2017).
[44]J. M. Larkin and A. J. McGaughey, Phys. Rev. B **89**(14), 144303 (2014).
[45]W. Zhu, G. Zheng, S. Cao, and H. He, Sci. Rep. **8**(1), 10537 (2018).
[46]W. X. Zhou, Y. Cheng, K. Q. Chen, G. Xie, T. Wang, and G. Zhang, Adv. Funct. Mater. **30**(8), 1903829 (2020).
[47]P. B. Allen and J. L. Feldman, Phys. Rev. B **48**(17), 12581 (1993).
[48]P. B. Allen, J. L. Feldman, J. Fabian, and F. Wooten, Philos. Mag. B **79**(11–12), 1715 (1999).
[49]J. L. Feldman, P. B. Allen, and S. R. Bickham, Phys. Rev. B **59**(5), 3551 (1999).
[50]I. Stark, M. Stordeur, and F. Syrowatka, Thin Solid Films **226**(1), 185 (1993).
[51]A. Cai, L.-P. Yang, J.-P. Chen, T.-G. Xi, S.-G. Xin, and W. Wu, J. Chem. Eng. Data **55**(11), 4840 (2010).
[52]A. Cappella, J. L. Battaglia, V. Schick, A. Kusiak, A. Lamperti, C. Wiemer, and B. Hay, Adv. Eng. Mater. **15**(11), 1046 (2013).
[53]S.-M. Lee, D. G. Cahill, and T. H. Allen, Phys. Rev. B **52**(1), 253 (1995).
[54]J. Paterson, D. Singhal, D. Tainoff, J. Richard, and O. Bourgeois, J. Appl. Phys. **127**(24), 245105 (2020).
[55]C. S. Gorham, J. T. Gaskins, G. N. Parsons, M. D. Losego, and P. E. Hopkins, Appl. Phys. Lett. **104**(25), 253107 (2014).
[56]J. T. Gaskins, P. E. Hopkins, D. R. Merrill, S. R. Bauers, E. Hadland, D. C. Johnson, D. Koh, J. H. Yum, S. Banerjee, B. J. Nordell, M. M. Paquette, A. N. Caruso, W. A. Lanford, P. Henry, L. Ross, H. Li, L. Li, M. French, A. M. Rudolph, and S. W. King, ECS J. Solid State Sci. Technol. **6**(10), N189 (2017).
[57]R. L. Xu, M. Muñoz Rojo, S. Islam, A. Sood, B. Vareskic, A. Katre, N. Mingo, K. E. Goodson, H. G. Xing, D. Jena, and E. Pop, J. Appl. Phys. **126**(18), 185105 (2019).
[58]R. Powell, R. Tye, and J. Woodman Margaret, Platinum Met. Rev. **6**(4), 138 (1962).
[59]L. Abadlia, F. Gasser, K. Khalouk, M. Mayoufi, and J.-G. Gasser, Rev. Sci. Instrum. **85**(9), 095121 (2014).
[60]H. Yokokawa and Y. Takahashi, J. Chem. Thermodyn. **11**(5), 411 (1979).
[61]A. D. Mah, W. Weller, and A. Christensen, *Thermodynamic Properties of Aluminum Nitride* (U.S. Department of the Interior, Bureau of Mines, 1961).
[62]R. B. Wilson and D. G. Cahill, Nat. Commun. **5**(1), 5075 (2014).
[63]C. Duquenne, M.-P. Besland, P. Tessier, E. Gautron, Y. Scudeller, and D. Averty, J. Phys. D: Appl. Phys. **45**(1), 015301 (2012).
[64]M. S. B. Hoque, Y. R. Koh, J. L. Braun, A. Mamun, Z. Liu, K. Huynh, M. E. Liao, K. Hussain, Z. Cheng, E. R. Hoglund, D. H. Olson, J. A. Tomko, K. Aryana, R. Galib, J. T. Gaskins, M. Elahi, Z. C. Leseman, J. M. Howe, T. Luo, S. Graham, M. S. Goorsky, A. Khan, and P. E. Hopkins, ACS Nano **15**(6), 9588 (2021).
[65]R. Rounds, B. Sarkar, A. Klump, C. Hartmann, T. Nagashima, R. Kirste, A. Franke, M. Bickermann, Y. Kumagai, Z. Sitar, and R. Collazo, Appl. Phys. Express **11**(7), 071001 (2018).

[66] S. Kumar and G. C. Vradis, J. Heat Transfer **116**(1), 28 (1994).
[67] A. F. Mayadas and M. Shatzkes, Phys. Rev. B **1**(4), 1382 (1970).
[68] A. F. Mayadas, M. Shatzkes, and J. F. Janak, Appl. Phys. Lett. **14**(11), 345 (1969).
[69] J. W. C. De Vries, J. Phys. F: Met. Phys. **17**(9), 1945 (1987).
[70] P. Nath and K. L. Chopra, Thin Solid Films **20**(1), 53 (1974).
[71] T. Q. Qiu and C. L. Tien, J. Heat Transfer **115**(4), 842 (1993).
[72] Q. G. Zhang, B. Y. Cao, X. Zhang, M. Fujii, and K. Takahashi, Phys. Rev. B **74**(13), 134109 (2006).
[73] B. Feng, Z. Li, and X. Zhang, Thin Solid Films **517**(8), 2803 (2009).
[74] J. W. C. De Vries, Thin Solid Films **150**(2–3), 201 (1987).
[75] J. W. C. De Vries, Thin Solid Films **167**(1–2), 25 (1988).
[76] R. K. Islamgaliev, N. A. Akhmadeev, R. R. Mulyukov, and R. Z. Valiev, Phys. Status Solidi A **118**(1), K27 (1990).
[77] M. R. Islam, P. Karna, J. A. Tomko, E. R. Hoglund, D. M. Hirt, M. S. B. Hoque, S. Zare, K. Aryana, T. W. Pfeifer, C. Jezewski, A. Giri, C. D. Landon, S. W. King, and P. E. Hopkins, Nat. Commun. **15**(1), 9167 (2024).
[78] C. Durkan and M. E. Welland, Phys. Rev. B **61**(20), 14215 (2000).
[79] A. Giri, M. V. Tokina, O. V. Prezhdo, and P. E. Hopkins, Mater. Today Phys. **12**, 100175 (2020).
[80] B. C. Gundrum, D. G. Cahill, and R. S. Averback, Phys. Rev. B **72**(24), 245426 (2005).
[81] A. Sytchkova, A. Belosludtsev, L. Volosevičienė, R. Juškėnas, and R. Simniškis, Opt. Mater. **121**, 111530 (2021).
[82] S. Srichandan, S. Wimmer, S. Pöllath, M. Kronseder, H. Ebert, C. H. Back, and C. Strunk, Phys. Rev. B **98**(2), 020406 (2018).
[83] C. Y. Ho, M. W. Ackerman, K. Y. Wu, S. G. Oh, and T. N. Havill, J. Phys. Chem. Ref. Data **7**(3), 959 (1978).
[84] C. Y. Ho, M. W. Ackerman, K. Y. Wu, T. N. Havill, R. H. Bogaard, R. A. Matula, S. G. Oh, and H. M. James, J. Phys. Chem. Ref. Data **12**(2), 183 (1983).
[85] J. P. Moore, T. G. Kollie, R. S. Graves, and D. L. McElroy, J. Appl. Phys. **42**(8), 3114 (1971).
[86] P. E. Hopkins, M. Ding, and J. Poon, J. Appl. Phys. **111**(10), 103533 (2012).